International Journal of Heat and Mass Transfer 52 (2009) 860–869

Contents lists available at ScienceDirect

International Journal of Heat and Mass Transfer

journal homepage: www.elsevier.com/locate/ijhmt

Modeling heat transfer in Bi_2Te_3–Sb_2Te_3 nanostructures

Arvind Pattamatta, Cyrus K. Madnia *

Department of Mechanical and Aerospace Engineering, State University of New York at Buffalo, 334 Jarvis Hall, Buffalo, NY 14260-4400, United States

ARTICLE INFO

Article history:
Received 29 October 2007
Received in revised form 16 May 2008
Available online 22 October 2008

Keywords:
Bi_2Te_3
Sb_2Te_3
Boltzmann equation
Nanostructures
Superlattice
Nanowire

ABSTRACT

Bi_2Te_3–Sb_2Te_3 nanostructures are gaining importance for use in thermoelectric applications following the finding that the Bi_2Te_3–Sb_2Te_3 superlattice exhibits a figure of merit, $ZT = 2.4$, which is higher than conventional thermoelectric materials. In this paper, thermal transport in the cross-plane direction for Bi_2Te_3–Sb_2Te_3 nanostructures is simulated using the Boltzmann transport equation (BTE) for phonon intensity. The phonon group velocity, specific heat, and relaxation time are calculated based on phonon dispersion model. The interfaces are modeled using a combination of diffuse mismatch model (DMM), and the elastic acoustic mismatch model (AMM). The thermal conductivity for the Bi_2Te_3–Sb_2Te_3 superlattice is compared with the experimental data, and the best match is obtained for specularity parameter, p, of 0.9. The present model is extended to solve for thermal transport in 2-D nanowire composite in which Sb_2Te_3 wires are embedded in a host material of Bi_2Te_3. Unlike in bulk composites, the results show a strong dependence of thermal conductivity, temperature, and heat flux on the wire size, wire atomic percentage, and interface specularity parameter. The thermal conductivity of the nanowire is found to be in the range of 0.034–0.74 depending on the atomic percentage and the value of p.

1. Introduction

Thermoelectric energy conversion is a field that can greatly benefit from the nanoscale heat transport phenomenon. The efficiency of thermoelectric conversion for a material is measured by a non-dimensional figure of merit (ZT) defined as, $ZT = \sigma S^2 T/k$ where σ is the electrical conductivity, S is the Seebeck coefficient, T is the temperature, and k is the thermal conductivity [1]. During the last decade, advances have been made in increasing ZT using nanostructures [2–7]. This was achieved by reducing the phonon thermal conductivity more than the electrical conductivity [8]. Although the decrease in thermal conductivity may be due to several effects such as the phonon group velocity reduction caused by the spectrum change, the interface thermal resistance and interface scattering, phonon interference and tunneling, and dislocations, it is found that scattering of energy carriers at interfaces plays the most important role [9]. The reduction in the effective thermal conductivity enhances the thermoelectric energy conversion.

The nanostructure configuration that show potential for enhancing ZT consists of multilayered thin films of different materials with thickness ranging from a monoatomic layer to thousands of angstroms called superlattice. Recent experimental studies [5,6] have demonstrated significant enhancement of ZT with Bi_2Te_3/Sb_2Te_3 superlattice in the cross-plane direction and PbTe/PbTeSe quantum dot superlattice along the film plane direction. Venkatasubramanian et al. [6] has reported a ZT of 2.4 for Bi_2Te_3–Sb_2Te_3 superlattice. However, superlattice grown by thin-film deposition techniques is not suitable for large scale applications due to its high manufacturing cost and difficulty to scale up for large scale applications. Nanocomposites offer a more economical alternative to superlattice in the quest for high ZT materials [10]. The features that make nanowire composites attractive for thermoelectric application are the 'size-effect' and 'effect of atomic percentage' which imply that the effective thermal conductivity of the nanowire depends on the material dimension as well as the atomic percentage of the wire. This remarkable feature of nanocomposites can be used to tailor the mechanical, thermal, and electrical properties which are best suited for a particular application.

Despite the importance of nanocomposites for thermoelectric applications, only a few experimental and numerical studies exist in the literature on the thermal characteristics of nanocomposites. Most of the computational studies on thermal transport using the particle based Boltzmann transport equation (BTE) have focused mainly on thin films, superlattices, and crystals [11–14]. Yang and Chen [15] have performed numerical simulations of cross-plane heat transport in a two-dimensional Ge–Si nanocomposite with an array of silicon wires embedded in a host material of Germanium. Yang et al. [16] report numerical simulation of Ge–Si core shell and tubular nanowires with heat transport along the axis of the wire. In both cases, the interfaces are treated as totally diffuse and their results show the effective thermal conductivity of the Ge–Si nanowire to be more than the superlattice for Si atomic percentage of 0.2. Recently, Prasher [17] has developed an analytical method for estimating the longitudinal thermal conductivity in nanowires and nanopores.

* Corresponding author. Tel.: +1 716 645 2593/2315; fax: +1 716 645 2883.
E-mail address: madnia@eng.buffalo.edu (C.K. Madnia).

0017-9310/$ - see front matter © 2008 Elsevier Ltd. All rights reserved.
doi:10.1016/j.ijheatmasstransfer.2008.09.004

Nomenclature

Chemical symbols

Bi_2Te_3	bismuth telluride
Ge	germanium
Sb_2Te_3	antimony telluride
Si	silicon

Roman symbols

a	lattice constant
AP	atomic percentage
C	volumetric specific heat (J/m^3 K)
D_p	density of states per unit volume (m^{-3})
f	phonon distribution function
$\hbar$	Planck's constant divided by 2π (1.054×10^{-34} J s/phonon)
I	phonon intensity (W m^{-2} sr^{-1})
I^*	non-dimensional phonon intensity
k	thermal conductivity (W/mK)
k_B	Boltzmann constant (1.38×10^{-23} J/K phonon)
Kn	Knudsen number (Λ/L)
L	material dimension
L_p	superlattice period thickness (m)
L_w	nanocomposite wire size (m)
$\vec{n}$	normal vector
N_ϕ	number of discrete azimuthal angular divisions
N_θ	number of discrete polar angular divisions
NC	nanocomposite
p	interface specularity parameter
q	heat flux (W/m^2)
Q_x	heat flow in the x-direction (W)
q_x^*	non-dimensional heat flux $[q_x/vC(\overline{T}(x = L_{Bi_2Te_3}) - \overline{T}(x = 0))]$
q_s	heat flux per solid angle (W m^{-2} sr^{-1})
$\vec{r}$	position vector
R_d	diffuse reflectivity
R_s	specular reflectivity
$\vec{s}$	phonon direction vector
S	Seebeck coefficient (μV/K)
SL	superlattice
T	absolute temperature (K)
$\overline{T}$	average temperature (K)
TBR	thermal boundary resistance
T_r	reference temperature (K)
T^*	non-dimensional temperature $[(T - T_r)vCL_{Sb_2Te_3}/Q_x]$
t	time (s)
T_d	diffuse transmissivity
T_s	specular transmissivity
U	volumetric internal energy (J/m^3)
V	volume (m^3)
v	average phonon group velocity (m/s)
w_θ	quadrature weight corresponding to the polar angle
w_ϕ	quadrature weight corresponding to the azimuthal angle
x	coordinate
y	coordinate
x^*	non-dimensional x-coordinate $[x/L_{Bi_2Te_3}]$
y^*	non-dimensional y-coordinate $[y/L_{Bi_2Te_3}]$
ZT	non-dimensional figure of merit

Greek symbols

β	grid compression factor
δ	interface roughness (m)
η	y-directional cosine
θ	polar angle (rad)
Λ	phonon mean free path (m)
λ	phonon wavelength (m)
μ	x-directional cosine
σ	electrical conductivity (S/m)
τ	frequency independent phonon relaxation time
ϕ	azimuthal angle (rad)
ω	phonon frequency (Hz)
ζ	acoustic impedance

Subscripts

b	boundary
c	phonon scattering
d	diffuse interface
eq	equilibrium
g	phonon generation
h	host (Bi_2Te_3)
i	interface
p	polarization mode
r	phonon reflection
s	specular interface
U	umklapp scattering
w	wire (Sb_2Te_3)
x	x-coordinate
y	y-coordinate

The main objective of the present work is to extend the general framework of thermal modeling of superlattice to simulate heat transport in Bi_2Te_3–Sb_2Te_3 nanowire composite. The heat transport in the cross-plane direction of Bi_2Te_3–Sb_2Te_3 superlattice is modeled and its thermal conductivity is compared with the experimental result [18]. The simulations are extended to Bi_2Te_3–Sb_2Te_3 nanowire composites, to understand the temperature and heat flux distributions as well as the effective thermal conductivity of such nanocomposites. The effects of the wire size, interface treatment, and atomic percentage on the thermal properties are also studied.

2. Problem description and modeling

The schematics of the superlattice and the 2-D nanowire composite chosen for the present simulations are shown in Fig. 1. The superlattice consists of periodically repeating stacks of Bi_2Te_3 on Sb_2Te_3 layers with heat transport across the layers. It is useful in studying the role of interface in the reduction of thermal conductivity.

The nanowire composite consists of an array of Sb_2Te_3 wires aligned parallel to each other and embedded in the host material of Bi_2Te_3, as shown in Fig. 1(b). Both the wires and the host are assumed to have a square cross-section. The heat transport is applied across the direction of the wire and there is no heat flow along the wire direction. This configuration mimics a thermoelectric device in which the wires are aligned for the device to transport the maximum heat flux perpendicular to the wire axis. Thus, a 2-D thermal energy transport is considered. For the ease of computations, the unit cell approach [19] shown in Fig. 1(c) is used to simulate the effect of a single wire and the surrounding host material within the cell.

To investigate the heat transfer in nanostructures, the main energy carriers in semiconductor materials namely phonons are modeled. Since the present study is conducted at room temperature, it is assumed that the short wavelength acoustic phonons contribute to the heat transfer. Hence, the wave nature of phonons is neglected and phonons are modeled as particles [20]. The

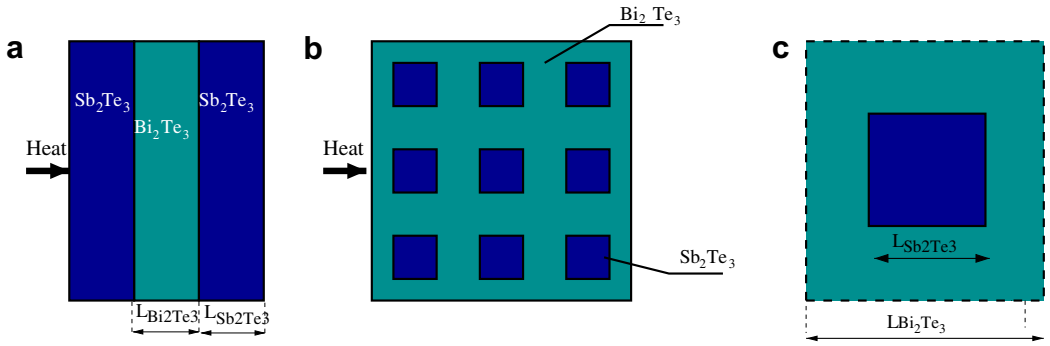

Fig. 1. Schematic of Bi_2Te_3–Sb_2Te_3: (a) superlattice, (b) 2-D nanowire composite, and (c) unit cell.

phonons are modeled via the BTE for the phonon intensity in the relaxation time approximation. This involves a simplification of the nonlinear scattering terms in the BTE through the introduction of the BGK approximation [21]. The relaxation time approximation does not take into account all the complex phonon–phonon scattering processes and neglects the inelastic interactions of phonons with other charge carriers. The intensity of phonon radiation, I, is defined as the flux of energy per unit time, per unit area, and per unit solid angle in the direction $\vec{s}$ and related to the phonon distribution function $f_p(\vec{r},\vec{s},t)$ as [22]

$$I(\vec{r},\vec{s},t)=\frac{1}{4\pi}\sum_{p=1}^{3}\hbar\omega\upsilon_p f_p(\vec{r},\vec{s},t)D_p(\omega) \tag{1}$$

where $\vec{r}$ denotes the phonon position vector, $\hbar$ is the Planck's constant divided by 2π, ω is the phonon frequency, υ_p is the phonon velocity corresponding to each polarization mode p, and $D_p(\omega)$ is the density of states per unit volume. The equilibrium distribution of phonons at temperature T is represented by the Bose–Einstein distribution [11].

For a two-dimensional system using the coordinate system shown in Fig. 2, the frequency independent BTE can be expressed as [15]

$$\frac{\partial I}{\partial t}+\upsilon\left(\mu\frac{\partial I}{\partial x}+\eta\frac{\partial I}{\partial y}\right)=\frac{I_{eq}-I}{\tau}\quad\text{where}\quad I_{eq}=\frac{1}{4\pi}\int_0^{2\pi}\int_{-1}^{1}I\,d\mu\,d\phi \tag{2}$$

where μ and η are the x- and y-direction cosines, respectively, and υ is the average phonon group velocity. The 'gray medium' BTE assumes frequency independent phonon relaxation time and group velocity, and hence does not account for interactions among phonons of different frequencies. In the present simulations, only the phonon–phonon Umklapp scattering time, τ, is considered.

The material properties used in the computation are evaluated using the phonon dispersion model proposed by Chen [23]. This model uses the frequency averaged specific heat and velocity to calculate the phonon mean free path from the relation

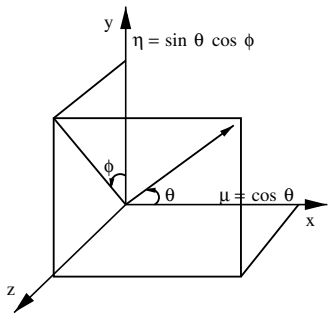

Fig. 2. Coordinate system used in the simulations.

$$k=\frac{\Lambda}{3}\sum_p\int_0^{\omega_{mp}}C_{\omega p}(\omega)\upsilon_p(\omega)\,d\omega \tag{3}$$

where ω_{mp} is the maximum allowable frequency corresponding to the polarization p and is related to the Debye temperature. The phonon dispersion relations for Bi_2Te_3 and Sb_2Te_3 [24] are obtained along the (1 1 1) crystal direction and are assumed isotropic in other directions. They are approximated as sine function similar to that of a linear atomic chain

$$\omega_p=\omega_{mp}sin\left(\vec{k}a/2\right) \tag{4}$$

where a is the equivalent atomic separation of an isotropic medium which can be determined from $a=\pi(6\pi^2/V)^{-\frac{1}{3}}$. Here, V is the volume of the Bi_2Te_3 or Sb_2Te_3 molecule. Both Bi_2Te_3 and Sb_2Te_3 crystals have two transverse and one longitudinal acoustic phonon modes. The two transverse modes are identical along the (1 1 1) direction for both crystals. For Bi_2Te_3, the Debye temperatures corresponding to the transverse and longitudinal acoustic phonons are 40 and 70 K respectively. For Sb_2Te_3, the Debye temperatures corresponding to the transverse and longitudinal acoustic phonons are 20 and 60 K respectively.

The group velocity and the specific heat for each polarization mode can be expressed as

$$\upsilon_p=\frac{\omega_{mp}a}{2}\cos\left(\frac{\vec{k}a}{2}\right) \tag{5}$$

$$C_{\omega p}=\frac{4\hbar^2}{\pi^2k_Ba^3T^2\omega_{mp}}\frac{\left[\sin^{-1}(\omega/\omega_{mp})\right]^2}{\cos\left(\vec{k}a/2\right)}\frac{\omega^2\exp\left(\hbar\omega/k_BT\right)}{\left[\exp\left(\hbar\omega/k_BT\right)-1\right]^2} \tag{6}$$

In the calculation of phonon group velocities, only the acoustic phonon contribution is accounted while neglecting the optical phonon contribution, since, the slopes of the optical phonon dispersion curves are small. The expression for the total specific heat is obtained by integrating the frequency dependant specific heat over the entire frequency range and summing over the acoustic polarization modes

$$C=\sum_p\int_0^{\omega_{mp}}C_{\omega p}\,d\omega \tag{7}$$

The mean free path can also be calculated from Eq. (3). The average group velocity of the phonons are calculated from the expression $k=\frac{1}{3}C\upsilon\Lambda$, using the bulk thermal conductivity, mean free path, and the total specific heat calculated from Eqs. (3) and (7).

The Debye model assumes a linear dispersion relationship between the phonon frequency and the wave vector. However, the phonon dispersion model takes into account the non-linear phonon dispersion and therefore gives a more accurate estimate of

the material properties. Table 1 summarizes the properties of Bi_2Te_3 and Sb_2Te_3 calculated at 300 K. The properties calculated using Debye model is also shown. The phonon properties obtained from Debye model are very different from the dispersion model.

3. Numerical methodology

The solution of BTE requires knowledge of the phonon relaxation time, the group velocity and the specific heat. Existing empirical models which describe the relaxation time as functions of frequency and temperature have been proposed for conventional semiconductor materials like silicon [22,25] but no such empirical models are available for Bi_2Te_3 and Sb_2Te_3. Therefore, a frequency independent relaxation time approach also referred to as the phonon gray medium approximation [15] is used in the present simulations.

The BTE for phonon intensity, in the relaxation time approximation along with its constituent boundary and interface conditions is solved to study the thermal characteristics of Bi_2Te_3–Sb_2Te_3 superlattices and nanocomposites. The first order upwind scheme is used for the spatial discretization of the BTE. Euler explicit time stepping method is used for temporal discretization to allow the solution to reach a steady state [26]. The angular discretization is performed through the decomposition of the polar and azimuthal angles into discrete directions such that $0 \leqslant \theta \leqslant \pi$ and $0 \leqslant \phi \leqslant \pi$ are discretized into N_θ and N_ϕ angular points, respectively. All angular integrations are performed using Gauss–Legendre quadratures [27], which discretizes the polar and azimuthal angles and assigns suitable weights for each direction. It has been shown that the use of Gauss–Legendre quadrature successfully resolves the 'ray effect' problem in phonon radiative transport [15].

In order to accurately capture the temperature jumps across the interfaces of the two materials, a non-uniform grid with a suitable compression [26] is used at all interfaces. A detailed spatial and angular grid resolution study is performed to test for grid independence of the solution. It is found that a spatial grid with 128×128 points and an angular decomposition with 30×20 points provide the best resolution of the thermal field. Since the code uses explicit Euler method for time stepping, a temporal resolution study has also been performed to determine the time step that ensures accurate transient solution.

The numerical solution to the BTE is computationally prohibitive on a single processor due to an excessive grid size of $128 \times 128 \times 30 \times 20$. Hence, the code has been parallelized using message passing interface (MPI) communication routines [28] and the parallel efficiency study indicates a near-linear scaleup from 2 to 64 processors. The parallel computations incur a CPU time per iteration per processor of 9 s on 64 processors.

4. Interface and boundary treatment

The BTE for the phonon intensity is solved in conjunction with suitable boundary and interface treatment. The treatment of interfaces between the two materials significantly affects the thermal characteristics of the nanostructure. For totally diffuse interfaces, the model proposed by Swartz and Pohl [29] called the diffuse mismatch model (DMM) is used. This model makes an assumption that the phonons emerging from an interface are independent of the phonons incident on the interface. The expression derived by Chen [9] which is valid for a wide temperature range is used to calculate the diffuse transmissivity. The transmissivity of phonons from Bi_2Te_3 side of the interface to Sb_2Te_3 side is calculated as

$$T_d(Bi_2Te_3 \rightarrow Sb_2Te_3) = \frac{U_{Sb_2Te_3} \upsilon_{Sb_2Te_3}}{U_{Bi_2Te_3} \upsilon_{Bi_2Te_3} + U_{Sb_2Te_3} \upsilon_{Sb_2Te_3}} \tag{8}$$

where U is the volumetric internal energy and υ denotes the phonon group velocity.

The specular scattering off an interface is modeled using the elastic acoustic mismatch model (AMM) [30]. The interface transmissivity from the Bi_2Te_3 side of the interface to the Sb_2Te_3 side and the reflectivity inside Bi_2Te_3 are given by the following relations:

$$T_s(Bi_2Te_3 \rightarrow Sb_2Te_3) = \frac{4\zeta_{Bi_2Te_3}\zeta_{Sb_2Te_3}\mu_{Bi_2Te_3}\mu_{Sb_2Te_3}}{\left(\zeta_{Bi_2Te_3}\mu_{Bi_2Te_3} + \zeta_{Sb_2Te_3}\mu_{Sb_2Te_3}\right)^2} \tag{9}$$

$$R_s(Bi_2Te_3) = 1 - T_s(Bi_2Te_3 \rightarrow Sb_2Te_3) \tag{10}$$

where ζ is the acoustic impedance of the material at the interface and μ is the x-direction cosine. It is assumed that the interface scattering process is elastic, i.e., the transmitted and reflected phonons have the same frequency as the incident phonons [31]. The incident and refracted angles obey the Snell's law of transmission. The equations for transmissivity and reflectivity of the AMM are valid only if the incident angle in Bi_2Te_3 is less than the critical angle, above which total internal reflection takes place such that $T_s(Bi_2Te_3 \rightarrow Sb_2Te_3) = 0$ and $R_s(Bi_2Te_3) = 1$.

The interfaces between the two materials are modeled as either totally diffuse or totally specular or as a combination of both [29,32]. The intensity of the phonons using the DMM for diffuse interfaces and AMM for specular interfaces are separately calculated and are combined using the interface specularity parameter p defined by Ziman [33] as

$$p = \exp\left(-\frac{16\pi^3\delta^2}{\lambda^2}\right) \tag{11}$$

where δ is the interface roughness and λ is the characteristic phonon wavelength. Zhang [34] presents this expression with π^2 in the exponent rather than the widely quoted π^3 as shown in Eq. (11). If the specularity parameter p is zero, it indicates a totally diffuse or a rough interface and a value of p equal to one indicates a specular or a smooth interface. A real interface is neither truly diffuse nor specular and hence cannot be accurately represented by the two limits. The interfaces can be modeled as diffuse if the interface roughness is greater than the phonon wavelength. However, for Bi_2Te_3, the phonon wavelength is 9 Å which is larger than a monolayer surface roughness of 2–3 Å. Even for values of interface roughness less than the phonon wavelength, Eq. (11) predicts a high probability for diffuse scattering. Therefore, the value of p is explicitly chosen to combine the diffuse and specular interface treatment models. As an example, consider the phonon intensity leaving the Sb_2Te_3 side of the interface. For a diffuse interface, from energy balance, the phonon intensity for $\theta > 0$, can be written as [15]

$$I_d(Sb_2Te_3) = \frac{2T_s(Bi_2Te_3 \rightarrow Sb_2Te_3)}{\pi}\int_0^{\pi}\int_0^{\pi/2} I_d(Bi_2Te_3)\cos\theta\sin\theta\,d\theta\,d\phi + \frac{2R_s(Sb_2Te_3)}{\pi}\int_0^{\pi}\int_{\pi/2}^{\pi} I_d(Sb_2Te_3)\cos\theta\sin\theta\,d\theta\,d\phi \tag{12}$$

For a specular interface, the energy balance of phonon intensity for a differential solid angle [23] can be written as

Table 1
Material properties

Material	Model	k (W/mK)	$C \times 10^6$ (J/m^3 K)	v (m/s)	MFP (Å)
Bi_2Te_3	Debye	1.1	1.22	2950	9.1
	Dispersion	1.1	0.5	212	310
Sb_2Te_3	Debye	0.9	1.32	3000	6.8
	Dispersion	0.9	0.53	200	254

$$I_s(Sb_2Te_3) = T_s(Bi_2Te_3 \rightarrow Sb_2Te_3) I_s(Bi_2Te_3) \times \left[\frac{\cos\theta_{Bi_2Te_3} \sin\theta_{Bi_2Te_3} d\theta_{Bi_2Te_3}}{\cos\theta_{Sb_2Te_3} \sin\theta_{Sb_2Te_3} d\theta_{Sb_2Te_3}}\right] + R_s(Sb_2Te_3) I_s(Sb_2Te_3) \quad (13)$$

The intensities obtained from the DMM and AMM are combined for a given value of p as [35]

$$I(Sb_2Te_3) = pI_s(Sb_2Te_3) + (1-p) I_d(Sb_2Te_3) \quad (14)$$

The equation for the intensity on the Sb_2Te_3 side of the interface reduces to diffuse interface model for $p = 0$ and the specular interface model for $p = 1$.

For the sake of computational simplicity, only a unit cell consisting of a single wire material of Sb_2Te_3 embedded in the Bi_2Te_3 host, Fig. 1(c), is modeled. The continuity of heat flow across the array of wires is modeled with the left and right boundaries of the unit cell as periodic interfaces. This ensures cell–cell interaction and thus the heat transport across the entire nanocomposite structure is represented by a single periodic cell. This boundary condition is also imposed on the superlattice to model the periodically repeating nature of the film stacks.

The periodic boundary condition implies that the perturbation of the intensity from its equilibrium value I_{eq} must be the same across the periodic boundaries to ensure the condition of constant heat flux. Mathematically, this can be expressed as

$$I(0,y,\theta,\phi) - I_{eq}(0,y) = I\left(L_{Bi_2Te_3}, y, \theta, \phi\right) - I_{eq}\left(L_{Bi_2Te_3}, y\right) \quad (15)$$

Using the relation between the equilibrium intensity I_{eq} and the equilibrium temperature (T), the above equation can be written as

$$I(0,y,\theta,\phi) - I\left(L_{Bi_2Te_3}, y, \theta, \phi\right) = \frac{C_{Bi_2Te_3} \upsilon_{Bi_2Te_3} \left(T(0,y) - T(L_{Bi_2Te_3}, y)\right)}{4\pi} \quad (16)$$

where C refers to the volumetric specific heat. The temperature difference across the periodic boundary $(T(0,y) - T(L_{Bi_2Te_3}, y))$ is fixed to a constant value of 1 K.

The adiabatic boundary condition is applied to the top and the bottom boundaries of the unit cell to ensure that the heat flows normal to the wire [15,35] as shown in Fig. 1(b). The adiabatic condition is modeled as a specularly reflecting boundary on which the following condition for intensity is imposed:

$$I_\omega(\vec{r}_b, \vec{s}, t) = I_\omega(\vec{r}_b, \vec{s}_r, t) \quad (17)$$

where $\vec{s}_r = \vec{s} - 2(\vec{s}\cdot\vec{n})\vec{n}$, $\vec{n}$ is the outward normal vector, and $\vec{r}_b$ denotes the spatial coordinates of the boundary.

5. Results and discussion

The parameters that affect the thermal characteristics of the superlattice and the nanowire composite are the Sb_2Te_3 film thickness for the superlattice and wire size $(L_{Sb_2Te_3})$ for the nanocomposite, atomic percentage of Sb_2Te_3, and the interface specularity parameter p.

The atomic percentage of the wire, AP, is related to the volumetric percentage of the wire, $V_{Sb_2Te_3}$, and the lattice constant, a, as [16]

$$AP = \frac{V_{Sb_2Te_3}}{\left(V_{Sb_2Te_3} + (1 - V_{Sb_2Te_3})\frac{a_{Sb_2Te_3}}{a_{Bi_2Te_3}}\right)} \quad (18)$$

For the nanowire composite, $V_{Sb_2Te_3} = \frac{L^2_{Sb_2Te_3}}{L^2_{Bi_2Te_3}}$, where $L_{Sb_2Te_3}$ and $L_{Bi_2Te_3}$ are the lengths of the wire and host, respectively.

For the nanocomposite, the effect of wire size is studied by fixing the atomic percentage while varying $L_{Sb_2Te_3}$. The effect of atomic percentage on thermal conductivity is studied by varying the wire atomic percentages for fixed wire sizes of 25.4, 254 and 2540 Å. The wire sizes 25.4, 254 and 2540 Å correspond to wire Knudsen number, Kn_w, of 10, 1 and 0.1, respectively. The Kn_w of 10 indicates ballistic transport inside the wire material, Kn_w of 0.1 indicates macroscopic regime and Kn_w of 1 indicates a transition regime. Each of these cases are modeled with specularity parameters of $p = 0$, 0.5, 0.8, 0.9 and 1, to study the effect of the interface treatment on the thermal characteristics of the nanostructures.

The phonon intensity obtained from solving the BTE is then used to determine the heat flux, temperature distribution, thermal conductivity, and thermal boundary resistance. At nanoscales, the temperature, as such, has no physical meaning except that it is an indicator of the local energy density of the system. Assuming constant specific heat, the effective temperature is obtained from phonon intensity as

$$T(x,y) = \frac{1}{C_{Bi_2Te_3} \upsilon_{Bi_2Te_3}} \sum_{N_\theta} \sum_{N_\phi} I(x,y,\theta,\phi) w_\theta w_\phi \quad (19)$$

where w_θ and w_ϕ are the weights associated with the polar and azimuthal directions, respectively. The heat fluxes in the *x*- and *y-directions* namely q_x and q_y are related to the intensity through the relations [15]

$$q_x(x,y) = \sum_{N_\theta} \sum_{N_\phi} I(x,y,\theta,\phi) \mu w_\theta w_\phi \quad (20)$$

$$q_y(x,y) = \sum_{N_\theta} \sum_{N_\phi} I(x,y,\theta,\phi) \eta w_\theta w_\phi \quad (21)$$

The effective thermal conductivity, k, can be defined as [15]

$$k = \frac{Q_x}{\overline{T}(x = L_{Bi_2Te_3}) - \overline{T}(x = 0)} \quad (22)$$

and the thermal boundary resistance (TBR) is given by

$$TBR = \frac{\overline{T}_i(Bi_2Te_3) - \overline{T}_i(Sb_2Te_3)}{Q_x} \quad (23)$$

where the heat flow $Q_x = \int_0^{L_{Bi_2Te_3}} q_x(x,y)\,dy$, $\overline{T} = \frac{1}{L_{Bi_2Te_3}} \int_0^{L_{Bi_2Te_3}} T(x,y)\,dy$ and $\overline{T}_i$ denotes the interface temperature.

5.1. Thermal characteristics of Bi_2Te_3–Sb_2Te_3 superlattice

The steady-state heat transport across the Bi_2Te_3–Sb_2Te_3 superlattice is examined. The dispersion model is used to obtain the phonon specific heat, velocity, and mean free path. Fig. 3 shows the effective thermal conductivity, k, calculated using Eq. (22), plotted as a function of the superlattice period thickness for the atomic percentage of 0.5. This figure shows a reduction in the thermal conductivity with decreasing period thickness of the superlattice. Here, the period thickness denotes the combined thicknesses of the two materials. This reduction is caused by the thermal boundary resistance to phonon transport, when the mean free path (MFP) of the phonons is greater than the half period thickness [29,31]. A study of varying the specularity parameter, p, is conducted to understand the effect of interface roughness on thermal conductivity of the superlattice. This study shows an increase in the thermal conductivity with increasing values of p. For diffuse interface, the phonon scattering occurs in all directions. Consequently, this causes a reduction in the heat flow and hence a smaller value of k is obtained. Whereas, in the case of $p = 1$, most of the scattering occurs along the heat flow direction resulting in higher value of k.

The experimental data of Venkatasubramanian [18] is also shown in Fig. 3. These data show a similar decrease in thermal

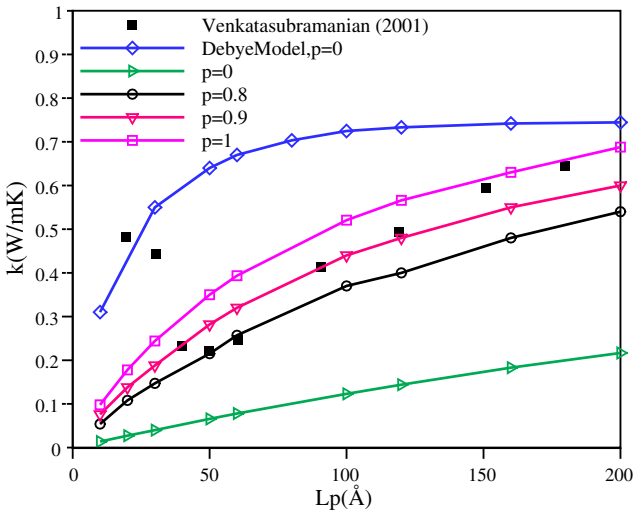

Fig. 3. Variation of thermal conductivity with period thickness for Bi_2Te_3–Sb_2Te_3 superlattice.

conductivity with reducing period thickness up to 50 Å. For thickness values less than 50 Å, the thermal conductivity increases and approaches the bulk value. Although the reasons for this behavior are not clear, some explanations pointing to the wave nature of phonons have been offered in the literature. One of them attributes this trend to phonon 'localization' effect [18]. The other explanation includes formation of phonon band structures due to coherent interference of phonon waves observed using lattice dynamics models [36]. Hence, phonon wave effects may become dominant for very small values of superlattice thicknesses. Since numerical simulation using the BTE assumes phonons as particles and excludes the wave effects, the present model cannot capture this trend observed in experiment.

The experimental data falls in between the specularity parameters $p = 0.8$–1 for a period thickness greater than 50 Å. Although, the experimental data are scattered within the band of 0.8–1, the predicted thermal conductivity for $p = 0.9$ gives the smallest root mean square (RMS) error of 15% when compared to data while, $p = 0$ shows the maximum error of 76%. This indicates that the actual interface scattering can neither be modeled as totally diffuse nor totally specular.

The thermal conductivity obtained using the dispersion model is compared with the Debye model for $p = 0$ in Fig. 3. The Debye model predicts thermal conductivity values which are not in accordance with the experimental data. This is due to MFP of the phonons calculated from the Debye model being smaller than the superlattice thickness, even for the period thickness of 50 Å. Consequently, the result with Debye model is closer to the macroscopic regime and cannot capture the ballistic effects observed in the experiment.

The predicted temperature profiles, not shown, are compared for different specularity parameters. For a fixed value of heat flux, the diffuse interface model shows a higher temperature jump at the interface and consequently Eq. (23) predicts a higher TBR for the diffuse interface model. Since, the TBR is inversely related to the thermal conductivity k, this results in a lower thermal conductivity for the diffuse interface.

5.2. Thermal characteristics of Bi_2Te_3–Sb_2Te_3 nanowire composite

Nanocomposite can be the practical alternative to superlattice for use in semiconductors and thermoelectric devices due to its scalability and lower manufacturing cost [10]. Superlattice construction requires extreme precision in aligning and stacking the films. For practical thermoelectric applications, nanocomposites are a better alternative from a mechanical as well as a thermo-electrical standpoint. This is because, the material properties in a nanocomposite can be tailored to achieve the desired thermal, electrical, and mechanical properties. In this section, the thermal characteristics of the Bi_2Te_3–Sb_2Te_3 nanowire composites are studied.

5.2.1. Temperature and heat flux

Fig. 4(a) and (b) shows the effective temperature, $T - T_r$, contours in the Bi_2Te_3–Sb_2Te_3 nanocomposite for an atomic percentage of $Sb_2Te_3 = 0.2$ and wire dimensions of $L_{Sb_2Te_3} = 25.4$ and 2540 Å, respectively. The reference temperature, T_r, is 300 K. The temperature contours for these wire sizes correspond to the ballistic regime ($Kn_w = 10$), for $L_{Sb_2Te_3} = 25.4$ Å, and the Fourier regime ($Kn_w = 0.1$), for $L_{Sb_2Te_3} = 2540$ Å. Here, Kn_w indicates phonon Knudsen number of the wire defined as the ratio of phonon mean free path to the wire size. Since the mean free path is different for the host and wire materials, the Knudsen numbers are defined separately for the materials based on their respective mean free path and dimensions. Thus for the Sb_2Te_3 wire, $Kn_w = \Lambda_{Sb_2Te_3}/(L_{Sb_2Te_3})$ and for the host material, Bi_2Te_3, $Kn_h = \Lambda_{Bi_2Te_3}/(L_{Bi_2Te_3} - L_{Sb_2Te_3})$.

From the temperature contours, it can be seen that for $L_{Sb_2Te_3} = 25.4$ Å, the interface scattering dominates the interior scattering of phonons and therefore the contours are clustered near the interfaces. The temperature contours for the case of $L_{Sb_2Te_3} = 2540$ Å are relatively uniform due to negligible interfacial scattering. The maximum and minimum temperatures occur at the interfaces for the ballistic case, and at the boundaries for the Fourier case.

To better understand the effects of scattering from the wire interfaces, the temperature profiles are plotted at three different

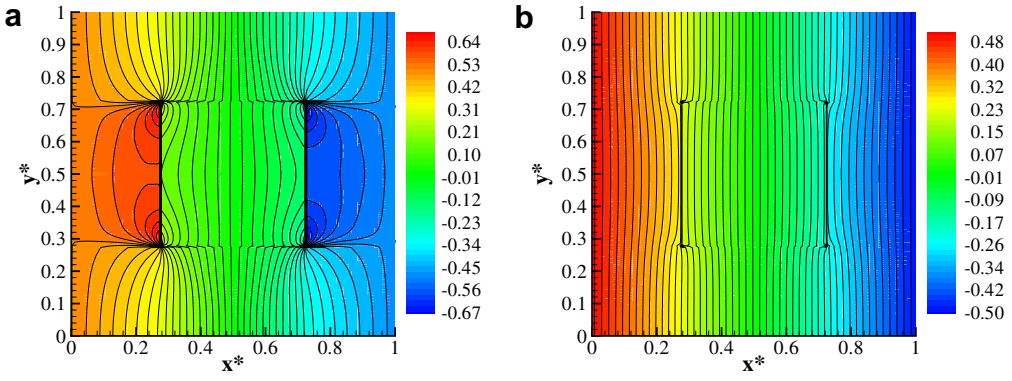

Fig. 4. Temperature ($T - T_r$) contours for atomic percentage of 0.2 with diffuse interfaces for $L_{Sb_2Te_3}$ (a) 25.4 Å and (b) 2540 Å.

y-locations. For an atomic percentage of 0.2, these are at halfway through the wire, denoted by $y^* = 0.5$, through the wire top interface at $y^* = 0.72$, and through the host material at $y^* = 0.85$. The y-locations are different for atomic percentage of 0.8. For this atomic percentage, the y-locations are at $y^* = 0.72$, $y^* = 0.95$ and $y^* = 0.99$, respectively.

Fig. 5 shows the temperature profiles plotted at the three y-locations described above. At each y-location, the temperature profiles are compared for atomic percentages of 0.2 and 0.8. For each atomic percentage, a comparison is made between the diffuse and specular interfaces. As can be seen from Fig. 5(a) and (b), temperature jumps occur at the interface between the host and wire and they can be attributed to interface thermal resistance. These jumps are not present in Fig. 5(c) due to the absence of any interface. The profiles corresponding to the wire top interface in Fig. 5(b) show larger temperature jumps at the interfaces as compared to the profiles at $y^* = 0.5$. For the atomic percentage of 0.2, at the locations along the wire midplane and the top interface, the left interface has a higher temperature, and the right interface has a lower temperature than the boundary temperature. There is a change in the sign of temperature gradient along the direction of heat flow which is similar to that obtained for the Ge–Si nanocomposite [15]. However, this is not observed for AP = 0.8.

The temperature profiles shown in Fig. 5, do not correspond to the same heat flow. Fig. 6 shows the non-dimensional temperature profiles, T^*, for the diffuse interfaces. For a fixed wire size, at the atomic percentage of 0.8, $Kn_h > Kn_w$. This implies that the host contributes to additional ballistic effects. Therefore, the interface scattering is more pronounced for the atomic percentage of 0.8 resulting in higher temperature jumps at the interfaces.

Fig. 7 shows the contours of normalized x-directional heat flux q_x^*, where q_x is the heat flux in the x-direction, for the atomic percentage of 0.2. The ballistic case of $L_{Sb_2Te_3} = 25.4$ Å shows an order of magnitude higher heat flux than the Fourier case of $L_{Sb_2Te_3} = 2540$ Å. The heat flux contours in the wire and host materials look very different for these cases. The location of the maximum heat flux is also different for the two cases. For the ballistic case, the maximum heat flux is located near the adiabatic boundaries on the top and bottom and away from the interfaces. For the Fourier case, the maximum heat flux is located at the interface corners. Unlike the temperature distribution, which displays even symmetry about the x-axis and odd symmetry about the y-axis, the heat flux contours show even symmetry about both x and y axes. The heat flow obtained by integrating the heat flux over a fixed x-plane, remains constant along the direction of heat transfer due to the periodic boundary conditions.

5.2.2. Thermal conductivity and figure of merit

In this section, the effects of the wire size, atomic percentage, and temperature on the effective thermal conductivity are discussed. Fig. 8(a) and (b) shows the variation of thermal conductivity for the nanowire and the superlattice with size, for atomic percentages of 0.2 and 0.8, respectively. Both specular and diffuse interfaces are examined. Unlike for the bulk composite, in which thermal conductivity does not vary with the physical dimensions, for nanocomposite it is size dependent. This dependence is called the 'classical size effect' which refers to the size effect attributed to the particle behavior of phonons. The variation in thermal conductivity with the wire size can be used to tailor the thermal properties of nanowire composites. This helps in achieving a better heat dissipation for nanoscale electronic devices and a more efficient thermal energy conversion for nanoscale thermoelectric devices.

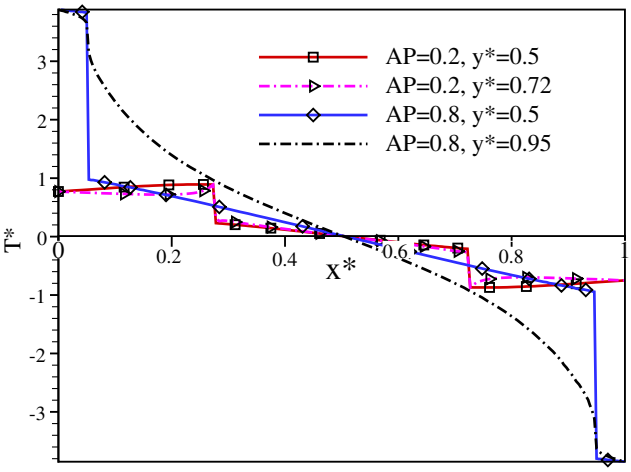

Fig. 6. Non-dimensional temperature profiles with diffuse interfaces.

Fig. 8 shows a decrease in the effective thermal conductivity of the nanowire, for both atomic percentages, with decreasing wire size. This decrease is due to the increase in phonon scattering at the interfaces with reduction in wire size. At room temperature, for wire sizes less than 25 Å, the wave effects may have to be considered in predicting the value of k. It is seen that for values of $L_{Sb_2Te_3}$ less than 100 Å, the values of superlattice and nanocomposite thermal conductivities are very close for both atomic percentages. However, a similar study conducted for the Ge–Si nanowire composite at AP = 0.2 and $p = 0$ predicted a higher value of k for the nanowire compared to the superlattice [15]. For larger wire sizes, the thermal conductivities of the nanowire composite and superlattice approach their respective bulk values; the bulk values of superlattice is lower than the nanowire composite. The superlattice has bulk thermal conductivity values of 1.17 and 1.11 corresponding to atomic percentages of 0.2 and 0.8, respectively, whereas the nanowire exhibits bulk values of 1.21 and 1.17, respectively. Comparison between Fig. 8(a) and (b) shows that for a given wire size, the thermal conductivity corresponding to AP = 0.8 is lower than that for AP = 0.2 due to increasing ballistic effects in the host.

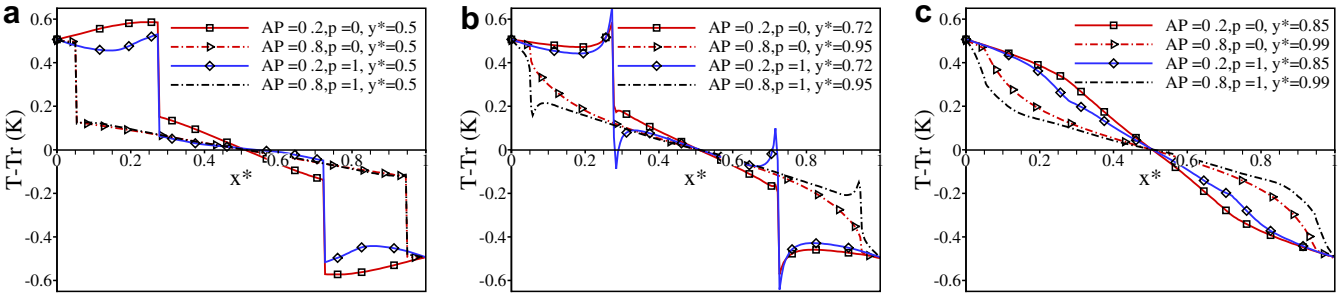

Fig. 5. Temperature profiles for $L_{Sb_2Te_3} = 25.4$ Å at section passing through (a) the center, (b) the wire top interface, and (c) the host.

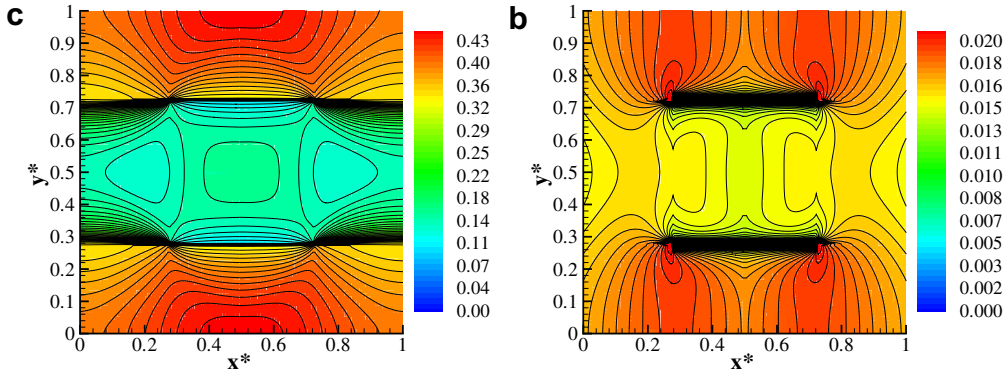

Fig. 7. Heat flux contours for atomic percentage of 0.2 with diffuse interfaces for $L_{Sb_2Te_3}$ (a) 25.4 Å and (b) 2540 Å.

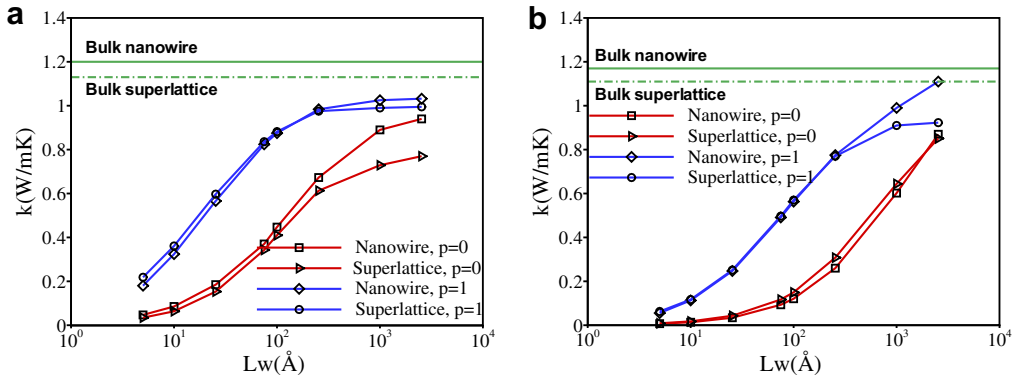

Fig. 8. Effect of wire size on thermal conductivity for Sb_2Te_3 atomic percentage of (a) 0.2 (b) 0.8.

Fig. 9(a) shows the effect of the atomic percentage on thermal conductivity for the ballistic case of $L_{Sb_2Te_3} = 25.4$ Å. The atomic percentage is varied from 0.1 to 0.9 and compared for the two interface specularity parameters of 0 and 1. Comparison of thermal conductivity of the nanowire is made with the superlattice. The thermal conductivity decreases with increasing atomic percentage. From Eq. (18), the volumetric percentage, $V_{Sb_2Te_3}$ increases with increasing atomic percentage. Consequently, the ballistic effects increase in the host. This results in a higher phonon interface scattering compared to the interior scattering, and hence a lower thermal conductivity. Therefore, for a fixed wire size, decreasing the host size lowers the thermal conductivity.

The effect of interface specularity parameter on the thermal conductivity can also be obtained from Figs. 8 and 9. Comparison between different values of p show that the diffuse interface results in thermal conductivity lower than the specular interface. Fig. 9(a) shows that the diffuse interface model predicts a higher thermal conductivity for the nanowire, for atomic percentages less than 0.4, and for larger values the nanowire and superlattice thermal conductivities become very close. The specular interface model, on the other hand, predicts slightly lower thermal conductivity for nanowire compared to superlattice.

The effect of reference temperature on thermal conductivity for the ballistic case is plotted in Fig. 9(b). The temperature dependent bulk thermal conductivity is used to calculate the corresponding phonon properties [24]. For $p = 0$, the thermal conductivity remains nearly constant, while for $p = 1$, the thermal conductivity

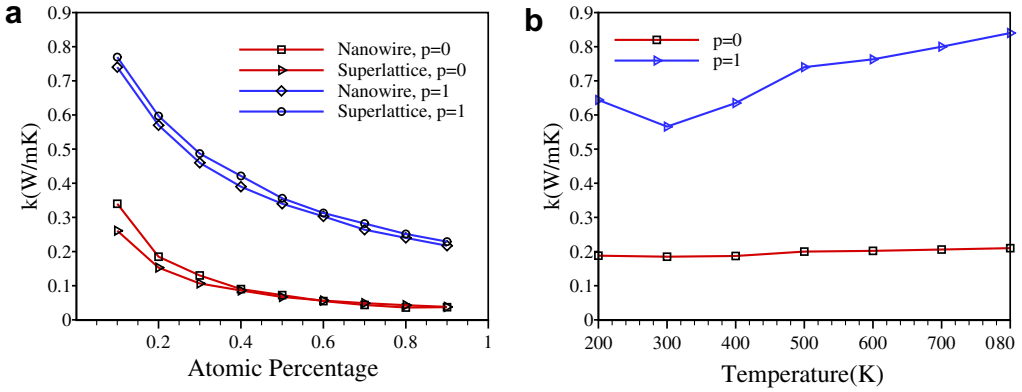

Fig. 9. Effect of (a) atomic percentage and (b) temperature on thermal conductivity for $L_{Sb_2Te_3} = 25.4$ Å.

Table 2
Thermoelectric properties of Bi_2Te_3–Sb_2Te_3 superlattice and nanowire composite

Material	Method	AP	p	k (W/mK)	$S^2\sigma$ (10^{-3} W/mK^2)	ZT
Bi_2Te_3–Sb_2Te_3 SL	Experiment [6]	0.5	–	0.22	1.76	2.4
Bi_2Te_3–Sb_2Te_3 SL	Simulation	0.5	0.9	0.28	1.76	1.89
Bi_2Te_3–Sb_2Te_3 NC	Simulation	0.5	0.9	0.26	1.76	2.03
Bi_2Te_3–Sb_2Te_3 NC	Simulation	0.1–0.9	0–1	0.034–0.74	1.76	0.71–15.5

increases with temperature and becomes larger than its value at room temperature.

Table 2 shows the comparison of thermoelectric properties and ZT for the superlattice and the nanowire composite. The wire size of the nanocomposite, for which the thermal conductivity is calculated, is 25 Å. This is equal to the thickness of Sb_2Te_3 at which the lowest thermal conductivity of 0.22 W/mK is observed experimentally [6]. The computed values of k corresponding to AP = 0.5 and p = 0.9 are 0.26 and 0.28 for the nanowire and superlattice, respectively. The value of p = 0.9 is chosen since the best match between the simulation and experiment for the superlattice is obtained for this value. The values of k for the nanowire composite vary between 0.034 and 0.74, depending on the atomic percentage and interface treatment. The electron properties such as the Seebeck coefficient and electrical conductivity may actually vary for the nanowire configuration. For the sake of comparison, we use the power factor of superlattice [6] to estimate the ZT for the nanowire. Thus, assuming a power factor, $S^2\sigma$, equal to the superlattice power factor, values of ZT in the range of 0.71–15.5 is obtained for the nanowire.

6. Summary and conclusions

The heat transport in the cross-plane direction for Bi_2Te_3–Sb_2Te_3 nanostructures has been studied by solving the Boltzmann transport equation (BTE) for phonon intensity in the relaxation time approximation. The phonon mean free path, group velocity, and specific heat are calculated from the phonon dispersion model. The interfaces are treated for specularity parameter, p, ranging from zero (totally diffuse) to 1 (totally specular), by a combination of the phonon intensity calculated using the diffuse mismatch model (DMM) and the elastic acoustic mismatch model (AMM). The motivation behind varying p is to gain understanding of the effect of interface roughness on the thermal conductivity of the nanostructure. This may be used to fabricate the material surfaces in experiments. For the superlattice, the calculated effective thermal conductivity is compared with the experiment [18]. The best match with the experimental data are obtained for specularity parameter, p, of 0.9. The increase in thermal conductivity at very small superlattice thickness observed in the experiment is attributed to phonon wave effects [18,36]. However, this cannot be captured in the present simulation by the particle model based BTE.

The computation for superlattice is extended to solve for the heat transfer in Bi_2Te_3–Sb_2Te_3 nanocomposite with Sb_2Te_3 wires embedded in the host material of Bi_2Te_3. The heat transfer is applied perpendicular to the axis of the wire and the nanowire is modeled as a unit cell with periodic boundaries. The effect of the nanocomposite wire size on the thermal characteristics is studied by varying the size of Sb_2Te_3 for a fixed atomic percentage. The effective thermal conductivity of the nanocomposite is found to be dependent on the wire size, unlike for the bulk composite. The thermal conductivity decreases with decreasing wire size and for very small sizes or large atomic percentages, the wave effects have to be considered. Comparison of the results for different interface treatments show that the diffuse interface model predicts thermal conductivity values of up to 2–4 times smaller than the specular interface model. The effect of Sb_2Te_3 atomic percentage on thermal conductivity is also studied. It is found that for a fixed wire size, increasing the atomic percentage of the wire results in lower thermal conductivity of the nanocomposite. The thermal conductivity of nanowire is found to be close to the superlattice. The thermal conductivity with diffuse interfaces is not very sensitive to the reference temperature in the range 200–800 K. The thermal conductivity of Bi_2Te_3–Sb_2Te_3 nanowire composite for the wire size of 25 Å at 300 K is in the range of 0.034–0.74 depending on the interface specularity parameter and the atomic percentage. The nanowire composite offers greater scalability than the superlattice due to phonon boundary scattering in multiple dimensions. Also, the nanocomposite is relatively more economical and suitable for thermoelectric applications that require tailored mechanical, electrical and thermal properties. These factors combined with the prospect of enhancing the ZT make the Bi_2Te_3–Sb_2Te_3 nanowire composite a suitable alternative to use in efficient thermoelectric applications.

Acknowledgments

We acknowledge funding support from the Donors of the Petroleum Research Funds administered by the American Chemical Society under Grant No. 41643-AC9. The authors thank Professor Theodorian Borca-Tasçiuc at RPI for his useful comments and discussions on the paper. The computational resources were provided by the National Center for Supercomputing Research (NCSA) under CTS030034N and by the Center for Computational Research (CCR) at SUNY-Buffalo.

References

[1] H. Goldsmid, Thermoelectric Refrigeration, Plenum Press, New York, 1964.
[2] M.S. Dresselhaus, Y.M. Lin, S.B. Cronin, O. Rabin, M.R. Black, G. Dresselhaus, T. Koga, Quantum wells and quantum wires for potential thermoelectric applications, Semiconduct. Semimet. 71 (2001) 1.
[3] M.S. Dresselhaus, G. Chen, M.Y. Tang, R. Yang, H. Lee, D. Wang, Z. Ren, J. Fleurial, P. Gogna, New directions for low-dimensional thermoelectric materials, Adv. Mater. 19 (2007) 1043–1053.
[4] W. Kim, J. Zide, A. Cossard, D. Klenov, S. Stemmer, A. Shakouri, A. Majumdar, Thermal conductivity reduction and thermoelectric figure of merit increase by embedding nanoparticles in crystalline semiconductors, Phys. Rev. Lett. 96 (2006) 045901-1–045901-4.
[5] T. Harman, P. Taylor, M. Walsh, B. LaForge, Quantum dot superlattice thermoelectric materials and devices, Science 297 (2002) 2229–2232.
[6] R. Venkatasubramanian, E. Colpitts, B. O'Quinn, Thin-film thermoelectric devices with high room-temperature figures of merit, Nature 413 (2001) 597–602.
[7] T. Borca-Tasciuc, D. Achimov, W. Liu, G. Chen, H. Ren, C. Lin, S. Pei, Thermal conductivity of In As/AlSb superlattices, Microscale Thermophys. Eng. 5 (2001) 225–231.
[8] R. Venkatasubramanian, Recent Trend in Thermoelectric Materials Research III: Semiconductors and Semimetals, Academic Press, San Diego, 2001.
[9] G. Chen, Thermal conductivity and ballistic transport in the cross-plane direction of superlattices, Phys. Rev. B 57 (1998) 14958–14973.
[10] G. Chen, Nanoscale heat transfer and nanostructured thermoelectrics, IEEE Trans. Component Packag. Technol. 29 (2006) 238–246.
[11] A. Joshi, A. Majumdar, Transient ballistic and diffusive phonon heat transport in thin films, J. Appl. Phys. 74 (1993) 31–39.
[12] M. Asheghi, M.N. Touzelbaev, K.E. Goodson, Y.K. Leung, S.S. Wong, Temperature dependent thermal conductivity of single-crystal silicon layers in SOI substrates, J. Heat Transfer 120 (1998) 30–33.
[13] P. Sverdrup, Y. Ju, K. Goodson, Sub-continuum simulations of heat conduction in silicon-on-insulator transistors, J. Heat Transfer 123 (2001) 130–137.
[14] A.J.H. McGaughey, M. Kaviany, Quantitative validation of the Boltzmann transport equation phonon thermal conductivity model under the single-

mode relaxation time approximation, Phys. Rev. B 69 (2004) 094303-1–094303-12.
[15] R. Yang, G. Chen, Thermal conductivity modeling of periodic two-dimensional nanocomposites, Phys. Rev. B 69 (2004) 195316-1–195316-10.
[16] R. Yang, G. Chen, M. Dresselhaus, Thermal conductivity of simple and tubular nanowire composites in the longitudinal direction, Phys. Rev. B 72 (2005) 125418-1–125418-7.
[17] R. Prasher, Thermal conductivity of composites of aligned nanoscale and microscale wires and pores, J. Appl. Phys. 100 (2006) 034307-1–034307-9.
[18] R. Venkatasubramanian, Lattice thermal conductivity reduction and phonon localizationlike behavior in superlattice structures, Phys. Rev. B 61 (2000) 3091–3097.
[19] J.D. Chung, M. Kaviany, Effects of phonon pore scattering and pore randomness on effective conductivity of porous silicon, Int. J. Heat Mass Transfer 43 (2000) 521–538.
[20] G. Chen, Nanoscale Energy Transport and Conversion: A Parallel Treatment of Electrons, Molecules, Phonons, and Photons, Oxford University Press, Oxford, 2005.
[21] P.L. Bhatnagar, E.P. Gross, M. Krook, A model for collision processes in gases. I. Small amplitude processes in charged and neutral one-component systems, Phys. Rev. 94 (3) (1954) 511–525.
[22] A. Majumdar, Microscale heat conduction in dielectric thin films, J. Heat Transfer 115 (1993) 7–16.
[23] G. Chen, Size and interface effects on thermal conductivity of superlattices and periodic thin-film structures, J. Heat Transfer 119 (1997) 220–229.
[24] O. Madelung, Semiconductors: Data Handbook, third ed., Springer, Berlin, 2004.
[25] M.G. Holland, Analysis of lattice thermal conductivity, Phys. Rev. 132 (1963) 2461–2471.
[26] K. Hoffmann, S. Chiang, Computational Fluid Dynamics for Engineers, Eng. Educ. Syst. (1993).
[27] W. Fiveland, Discrete ordinate methods for radiative heat transfer in isotropically and anisotropically scattering media, J. Heat Transfer 109 (1987) 809–812.
[28] W. Gropp, E. Lusk, A. Skjellum, Using MPI Portable Parallel Programming with the Message-Passing Interface, MIT Press, Cambridge, MA, 1997.
[29] E. Swartz, R. Pohl, Thermal boundary resistance, Review, Mod. Phys. 61 (1989) 605–668.
[30] W. Little, The transport of heat between dissimilar solids at low temperatures, Can. J. Phys. 37 (1959) 334–349.
[31] T. Zeng, G. Chen, Phonon heat conduction in thin films: Impacts of thermal boundary resistance and internal heat generation, J. Heat Transfer 123 (2001) 340–347.
[32] T. Klitsner, J.V. Cleve, H. Fischer, R. Pohl, Phonon radiative heat transfer and surface scattering, Phys. Rev. B 38 (1988) 7576–7594.
[33] J. Ziman, Electrons and Phonons, Oxford University Press, London, UK, 1960.
[34] Z. Zhang, Nano/Micro Scale Heat Transfer, McGraw-Hill, New York, 2007.
[35] A. Pattamatta, C. Madnia, Modeling thermal transport in two-dimensional nanocomposites, in: Bulletin of American Physical Society, 59th Annual Meeting of the Division of Fluid Dynamics of the American Physical Society, Tampa Bay, Florida, November 19–21, vol. 51, 2006, p. 110.
[36] B. Yang, G. Chen, Partially coherent phonon heat conduction in superlattices, Phys. Rev. B 67 (2003) 195311-1–195311-4.